OPEN ACCESS
IOP Publishing
Superconductor Science and Technology
Supercond. Sci. Technol. **36** (2023) 045008 (11pp)
https://doi.org/10.1088/1361-6668/acb857

Analysis of inhomogeneities in Nb_3Sn wires by combined SEM and SHPM and their impact on J_c and T_c

S Pfeiffer[1,3,*], T Baumgartner[2], S Löffler[1], M Stöger-Pollach[1], S C Hopkins[3], A Ballarino[3], M Eisterer[2] and J Bernardi[1]

[1] USTEM, TU Wien, Wiedner Hauptstraße 8-10, 1040 Vienna, Austria
[2] Atominstitut, TU Wien, Stadionallee 2, 1020 Vienna, Austria
[3] CERN, 1211 Geneva 23, Switzerland

E-mail: stephan.pfeiffer@tuwien.ac.at

Received 23 November 2022, revised 23 January 2023
Accepted for publication 2 February 2023
Published 24 February 2023

Abstract

We demonstrate the combined use of scanning electron microscopy (SEM) and scanning Hall probe microscopy (SHPM) to analyse inhomogeneities in Nb_3Sn wires. Inhomogeneities of the A15 phase in Nb_3Sn sub-elements of a Ti-alloyed Restacked Rod Process wire and a Ta-alloyed Powder-In-Tube wire are investigated. Microstructural features are examined by SEM, elemental concentration gradients by energy dispersive x-ray spectroscopy (EDX) and the superconducting properties by SHPM. Correlations between the results are analysed to gain information about the impact of inhomogeneities in the microstructure on the superconducting properties. We find considerable differences in geometry and performance between sub-elements, as well as compositional and geometric inhomogeneities of the A15 phase inside single sub-elements. Additionally, simulations of the influence of Sn concentration gradients on the critical current density J_c are performed. We also demonstrate the viability of SHPM and EDX for determining the dependence of the critical temperature T_c on the Sn concentration and discuss possible performance gains by a reduction of inhomogeneities in Nb_3Sn wires.

Keywords: Nb_3Sn, FCC, inhomogeneity, SEM, SHPM, microstructure

(Some figures may appear in colour only in the online journal)

1. Introduction

The current target baseline for FCC-hh accelerator dipole magnets based on Nb_3Sn superconductors is a non-Cu critical current density J_c of 1500 A mm^{-2} at 16 T and 4.2 K [1]. State-of-the-art Nb_3Sn wires do not reach this performance; a further J_c increase of 50% is required. In order to improve the manufacturing of Nb_3Sn wires, a deep understanding of the microstructure and its impact on the performance is necessary. Simulations in past studies have shown that compositional inhomogeneities in Nb_3Sn wires can have a great influence on the superconducting properties [2, 3], hence their investigation in industrial wires is important to assess potential performance gains.

In the present study, inhomogeneities are examined using experimental methods on state-of-the-art wires in order to gain a better understanding of their impact on the superconducting properties of real wires. The nature of these inhomogeneities are multifold and include geometric and compositional inhomogeneities as well as those in the local superconducting properties. We investigate the microstructure by scanning

* Author to whom any correspondence should be addressed.

electron microscopy (SEM), elemental concentration gradients by energy dispersive x-ray spectroscopy (EDX), and J_c and T_c by scanning Hall probe microscopy (SHPM).

The goals of the study are twofold: firstly, the conceptual introduction of the combined use of the given methods, and secondly the application of this approach to two different wire architectures. It has to be noted that these methods of analysing inhomogeneities yield information about local properties and are not designed for analysing the global properties, which might show considerably different values. Additionally, the combined investigation by SHPM and SEM of multiple sub-elements as well as the correlation between the results of both methods is extremely time-consuming and can therefore not easily be conducted on multiple cross sections per wire. Nevertheless, the combination of these methods allows a direct comparison and correlation between microstructural features and their influence on the local superconducting properties and can thus yield useful information about possible performance gains.

2. Experiments and simulations

We investigated inhomogeneities of sub-elements in two types of Nb_3Sn wires, a Ti-alloyed Restacked Rod Process (RRP®) wire with 108 sub-elements, subsequently denoted as RRP-Ti, and a Ta-alloyed powder-in-tube (PIT) wire with 114 filaments, denoted as PIT-Ta. For simplicity and ease of comparison, the term sub-element will be used here both for RRP sub-elements and PIT filaments. PIT and RRP type wires are currently the best candidates of standard wires for the use in future accelerator dipole magnets [1], hence the investigations were carried out on these wire types. An overview over the relevant properties of the investigated wires can be found in table 1.

One transversal cross section of each of the two different types of Nb_3Sn wires was polished for SEM and SHPM analysis, of which multiple sub-elements were investigated. Additionally, one sample of the RRP-Ti wire was prepared by polishing along the wire axis to the centre of a sub-element in order to examine longitudinal variations of the geometry and composition. Overview SEM images of all prepared and investigated samples can be found in figure 1.

2.1. SEM analysis

SEM imaging was performed using an FEI Quanta 250 FEG SEM to gain information about geometric variations of the A15 phase inside individual sub-elements and between different sub-elements. SEM images taken with the backscattered electron (BSE) detector were used to quantify the size distributions and aspect ratios of the sub-elements. The BSE detector yields high contrast between the Cu, Nb and A15 phases due to their differing atomic numbers. Based on the high contrast, the total area of the A15 phase and the inner parts of sub-elements of the RRP-Ti and PIT-Ta wires was evaluated by pixel counting.

Table 1. Relevant parameters of the investigated Nb_3Sn wires.

Sample	RRP-Ti	PIT-Ta
Type	RRP	PIT
Additive element	Ti	Ta
Additive content	2 at.%	5 at.%
Number of Subel.	108	114
Diameter	0.8 mm	0.7 mm
Cu/non-Cu ratio	1.02	1.21
Manufacturer	Bruker OST	Bruker EAS
Heat treatment	210 °C (48 h)	620 °C (120 h)
	400 °C (48 h)	640 °C (120 h)
	665 °C (50 h)	

2.2. EDX analysis

EDX analyses were carried out on the A15 layers of the sub-elements to gain information about the distribution of the elements. EDX line scans from the outside to the inside of the sub-elements were performed on the transversal cross sections with a step width of 100 nm to determine the radial variations of the Sn concentration. Additionally, the elemental composition of the A15 phase was measured along the wire axis with a step width of 200 nm to assess possible longitudinal variations of the Sn content. An accelerating voltage of 10 kV was used for the EDX analyses. In Nb_3Sn, this corresponds to a penetration depth of a few hundred nm [4], therefore the information acquired stems from the region between the sample surface and this depth. For quantification of the elemental contents, the Nb L, Sn L, Cu L, Ti K and Ta M peaks of the EDX spectra were used.

2.3. SHPM analysis

SHPM allows spatially resolved mapping of a magnetic field above a superconductor and was performed on the polished transversal cross sections of the RRP-Ti and the PIT-Ta wire in the remanent and Meißner states. The employed scanner is able to analyse a sample area of 3 mm × 3 mm with a resolution of 1 μm. The remanent field scans performed at 10 K after applying and deactivating a field of 1 T were used for calculating the critical current density J_c of the A15 layer of different sub-elements and comparing the resulting values.

In addition, SHPM was used to analyse differences in the critical temperature T_c of individual sub-elements by acquiring scans in the Meißner state at an applied external field of 5 mT. These scans were also used to evaluate the shielded area of the sub-elements at different temperatures. The SHPM scans were acquired without current injection to the samples. The pattern of currents and fields during current injection would differ from the employed setup.

2.4. Correlation of the SEM, EDX and SHPM results

The correlations between the results of the SEM, EDX and SHPM investigations were analysed; in particular, Hall scans of the remanent field in the RRP-Ti wire were compared with geometric information acquired by SEM. The area of each

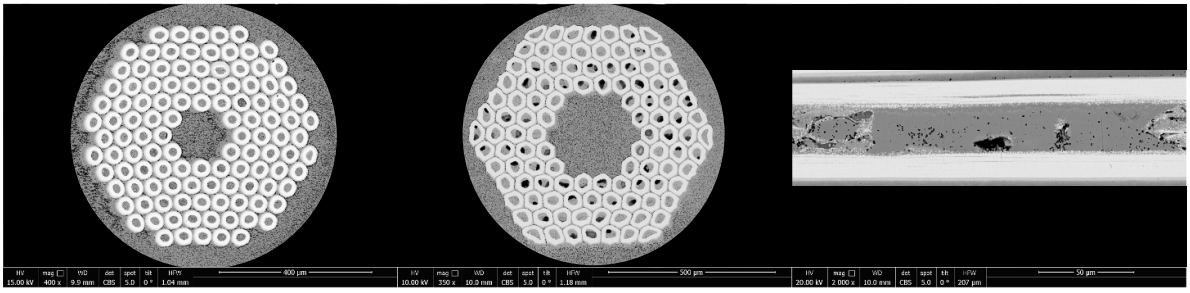

Figure 1. Overview SEM images taken with the BSE detector of the prepared and investigated samples. Polished transversal cross sections of the PIT-Ta wire (left) and the RRP-Ti wire (middle) as well as the longitudinal cross section of an RRP-Ti sub-element (right).

sub-element measured was determined by pixel counting from SEM images and the inner and outer radii were calculated based on circles with equivalent area. The critical current density J_c of the A15 layer was calculated from the central value of the remanent field above each sub-element.

Differences in the critical temperature T_c between individual sub-elements of the RRP-Ti wire that were determined by SHPM were compared with the Sn distribution in the A15 phase that was acquired by EDX in order to investigate the correlation between T_c and the Sn content in specific sub-elements.

The radii of the shielded areas of the sub-elements in the Meißner state at different temperatures were combined with EDX measurements of the Sn gradient across the A15 phase, yielding the general dependence of the critical temperature T_c on the Sn content.

The methods applied on the RRP-Ti wire in the first part of this study focus on evaluating differences between sub-elements across the wire cross section, while the analysis focused on the PIT-Ta wire in the second part aims to establish statistics over multiple sub-elements, and is thus representative of the average value of each sub-element across the wire section. The reason for the difference in methods applied to the two different wire types can be related to their better suitability for each method, since the PIT wire analysed in this study exhibited a greater homogeneity due to its manufacturing process of using Nb tubes instead of stacked filaments.

2.5. Simulations

Numerical simulations were carried out to evaluate the influence of the Sn concentration gradient inside the A15 phase of the sub-elements on the critical current density J_c. These simulations, which are described in detail in [3], use Sn concentration profiles and grain size profiles as an input. They are based on the Li–Gao model for calculating T_c and B_{c2} as a function of Sn content [5], and on the influence of the grain size on J_c described in [6]. Since the effects of additives on J_c are not included in the simulations for lack of a sufficiently accurate model, the maximum Sn content (in the centre of each sub-element) had to be adjusted to achieve a good match between the simulated and the experimentally observed $J_c(B,T)$. Using this matched profile as a starting point, the influence of the Sn concentration gradient was studied by changing the gradient relative to the original profile and comparing the resulting J_c values.

3. Results and Discussion

3.1. Sub-element area and aspect ratio distribution

The sub-element area and aspect ratio distributions of the RRP-Ti and PIT-Ta wire obtained using SEM imaging are shown together with their respective statistics in figures 2 and 3, where the sub-element area is defined as the total area of the A15 phase and the central area. The sub-elements were colour coded according to the measured values using the ROI Colour Coder plugin for the ImageJ program [7], where the colour bar ranges from the minimum to the maximum of the measured values, except for the aspect ratio of the RRP-Ti wire, where the upper limit was set to 1.35 due to the 6 outermost sub-elements being outliers with a maximum of 1.72. The opacity of the overlay was set to 80%, allowing the spatial extent of the A15 phase to be visible in the background. The colour in the central area of each sub-element corresponds to the value displayed by the colour bar. The sub-element area distributions of both wires can be approximated by Gaussian fits. The fits are marked by the red lines and the insets show the minimum, maximum, mean value and standard deviation of the experimental data.

It is clearly visible that there are significant variations of the sub-element areas and aspect ratios over the wire cross section. While no apparent correlation between location and geometry of the sub-elements can be found in the RRP-Ti wire, the outermost sub-elements are generally more elliptical than the ones near the wire centre in the PIT-Ta wire. The values of the sub-element areas show variations of up to 20%.

One sub-element in the PIT-Ta wire is worth mentioning as it has not reacted properly during heat treatment and exhibits only a very limited A15 fraction. This sub-element can be seen near the top of the wire cross section in figure 3 and was not included in the analysis.

3.2. Remanent fields and correlation with the microstructure

A Hall scan of the remanent field of the RRP-Ti wire was acquired at 10 K after applying and deactivating an external field of 1 T. The result can be found in figure 4, where a unique

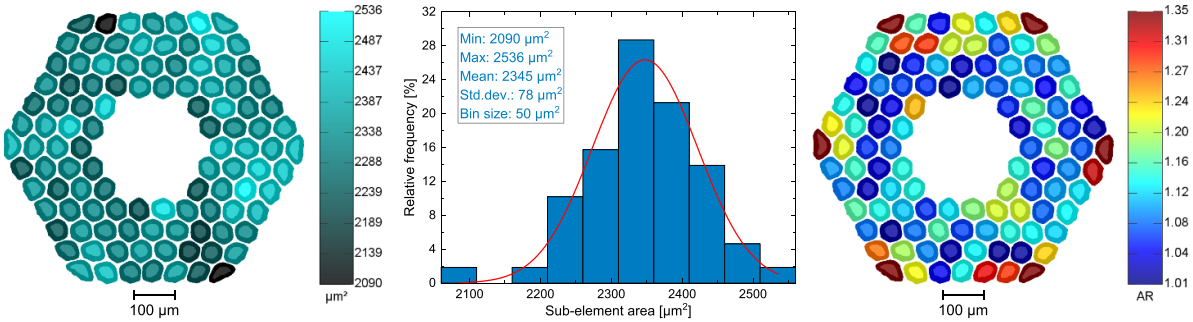

Figure 2. Areas of sub-elements in the RRP-Ti wire (left), statistics of sub-element area distribution of RRP-Ti wire (middle) and aspect ratios of sub-elements (right). The fit is marked by the red line and the inset shows the minimum, maximum, mean value and standard deviation of the experimental data.

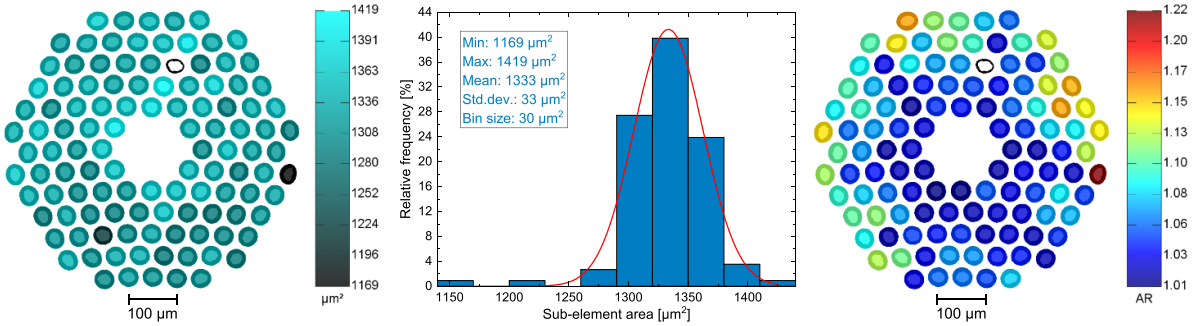

Figure 3. Areas of sub-elements in the PIT-Ta wire (left) and statistics of sub-element area distribution of PIT-Ta wire (middle) and aspect ratios of sub-elements (right). The fit is marked by the red line and the inset shows the minimum, maximum, mean value and standard deviation of the experimental data.

number was allocated to each sub-element. It becomes apparent that there are considerable differences in the magnitude and shape of the remanent fields between sub-elements.

After examination of the sub-elements by SHPM, SEM images of the same area as shown in figure 4 were taken in order to investigate a possible correlation between the remanent field and the geometry. This understanding is important for calculating J_c of the sub-elements as described in section 3.3. Figure 5 shows an overview image of the investigated sub-elements together with the evaluation of their area and aspect ratio. All relevant parameters of the investigated sub-elements are summarized in table 2.

As examples, sub-elements number 1, 4, 8 and 15 show low remanent fields as seen in figure 4 and rather small areas, while the aspect ratio seems to have no significant impact on the remanent field. Sub-elements number 10–14 show the highest remanent fields but simultaneously a large variation in area and aspect ratio. Sub-element number 8 exhibits an exceptionally low remanent field. When looking at figure 5, it becomes apparent that this sub-element seems to possess a smaller minimum thickness of the A15 phase than the remaining sub-elements. This suspicion was confirmed by analysing the minimum distance between the outer and inner border of all sub-elements using the layer thickness and line colour plugins for ImageJ [8]. The results of sub-elements number 8 and 9 are displayed in figure 6, where lines of the closest distance were drawn from each pixel at the outer border of the A15 layer to the inner border and coloured according to their length. The inner border of the A15 phase is often not clearly defined due to weakly connected grains, which complicates the evaluation of the A15 layer thickness.

It can be seen that the A15 layer thickness of sub-element number 8, which showed the lowest remanent field, at some locations only measures about 7.2 μm, which is 50% lower than the maximum value of the same sub-element. For comparison, sub-element number 9 shows a much more uniform distribution of the A15 layer thickness, which for the most part exceeds 10 μm with a minimum of 9.7 μm.

These findings show evidence that the minimum A15 layer thickness, further denoted as d_{A15}, has a major impact on the resulting remanent field, which needs to be considered for calculating J_c. This result is comprehensible, as the field of a long hollow cylinder is mainly dependent on the product between J_c and the wall thickness, where the radius only has a minor impact. It also implies that the aspect ratio does not significantly impact the field, as long as J_c stays constant.

The smallest wall or layer thickness d_{A15} therefore limits the circular currents locally and, as a result, the remanent field. It is important to note that such local variations can be the limiting factor for the performance of long wires. In practical wires, where the current flows in the longitudinal direction, variations of the A15 geometry limit the current by reducing the transverse superconducting cross section.

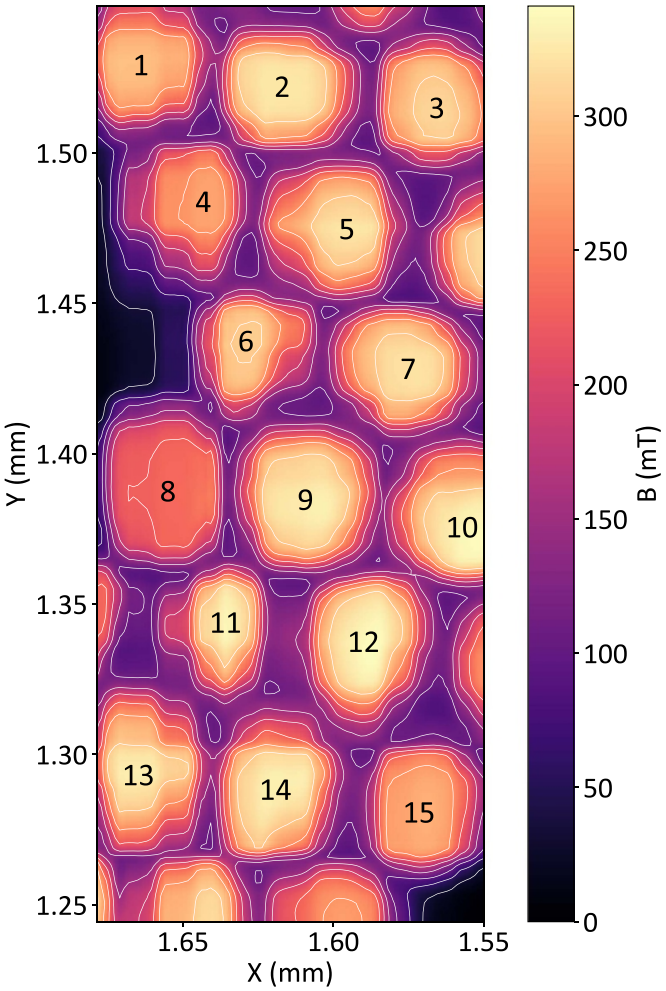

Figure 4. Remanent field Hall scan of the RRP-Ti wire at 10 K after applying and deactivating an external field of 1 T.

3.3. Determination of the sub-element J_c

The SHPM scan of the RRP-Ti wire in figure 4 was used to evaluate the critical current density J_c of the A15 layer of each sub-element, which can be calculated from the measured remanent magnetic flux profile by the inversion of the Biot–Savart law. For this, the sub-element geometry is approximated by a hollow cylinder as derived from [9].

While an uncertainty of a few μm in the distance of the Hall probe from the sample surface z can have a large impact on the result of J_c, the sample thickness t only significantly impacts the result below a value of about 50 μm for the present geometry. The Hall probe distance from the sample surface z was measured at multiple points to ensure a flat sample surface and an accurate determination of its value. For the SHPM measurements of the RRP-Ti wire the sample thickness t was about 3 mm and the Hall probe distance from the sample surface z was 2 μm. In the present case of large t and given the above assumptions, the equation for calculating J_c along the cylinder axis simplifies to

$$J_c = \frac{2B_z}{\mu_0 \left[r_o - r_i + z \ln\left(\frac{r_i + \sqrt{r_i^2 + z^2}}{r_o + \sqrt{r_o^2 + z^2}} \right) \right]}. \quad (1)$$

In equation (1), B_z denotes the measured remanent magnetic field in the sub-element centre, z the distance of the Hall probe from the sample surface, r_o the outer radius of the A15 phase and r_i the inner radius of the A15 phase.

In section 3.2, it was shown that the minimum A15 layer thickness d_{A15} has a major influence on the remanent field of the sub-elements. For that reason, r_o was determined by pixel counting of SEM images, while r_i was defined as the difference between the outer radius and the minimum A15 thickness, $r_i = r_o - d_{A15}$. The measured values of B_z, r_o, d_{A15} and the calculated critical current density J_c of the A15 layer of the investigated sub-elements can be found together with the measured values of their areas and aspect ratios in table 2.

It becomes apparent that individual sub-elements show considerable differences in geometry and remanent field values, resulting in different calculated J_c values, ranging from 5.39×10^4 A mm^{-2} to 6.62×10^4 A mm^{-2}. Sub-element number 4 possesses the lowest calculated J_c value and one of the smallest measured areas. Sub-element number 14 exhibits a high remanent field but a rather small d_{A15}, resulting in the highest calculated J_c value. The average value is 5.99×10^4 A mm^{-2} with a standard deviation of 0.32×10^4 A mm^{-2}. Therefore the maximum J_c value of 6.62×10^4 A mm^{-2} differs from the average value by about 10% and from the minimum value by about 20%.

Part of the variations of the calculated J_c can be attributed to the fact that equation (1) assumes a circular shape of the sub-elements and therefore might lead to errors in the calculation of J_c of elongated sub-elements. On the other hand, as expected no significant influence of the aspect ratio on the resulting remanent field was determined, therefore not affecting the calculation.

The average longitudinal self-field J_c of 8 pieces cut from the RRP-Ti wire was obtained from SQUID magnetometry at the same temperature of 10 K and evaluated based on the Bean model for hollow cylinders parallel to the field, similarly as described in [10] for transversally applied fields. It is quite remarkable that this analysis leads to $6.18(16) \times 10^4$ A mm^{-2}; thus the circular currents assessed by SHPM seem quite representative of the longitudinal currents.

Despite this good agreement it has to be noted that the obtained values by SHPM are based on local evaluations, and the ones by SQUID on samples of a few mm in length. It cannot be assumed that these values coincide with transport J_c values over km of length, or are representative of the global properties. One reason for that are longitudinal variations in the geometry and composition that will be discussed in section 3.6.

3.4. Differences in the sub-element T_c

Differences in the critical temperature T_c of individual sub-elements of the RRP-Ti wire were assessed by performing

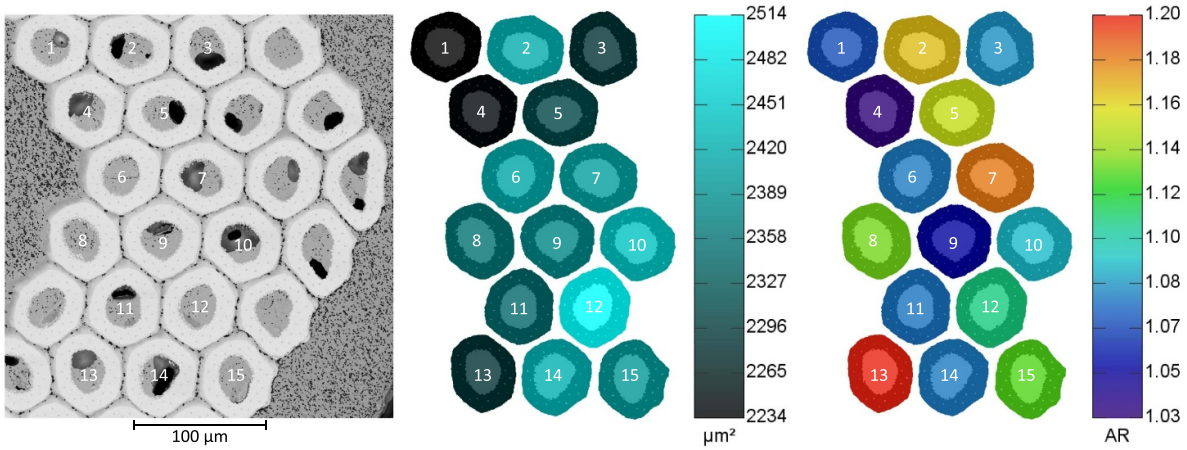

Figure 5. SEM image taken with the BSE detector of the investigated sub-elements of the RRP-Ti wire (left), their areas (middle) and their aspect ratios (right). The colour in the sub-element centre corresponds to the value in the colour bar.

Table 2. Comparison of the properties of the investigated RRP-Ti sub-elements.

Sub-element	B_z (mT)	r_o (μm)	d_{A15} (μm)	r_i (μm)	Area (μm^2)	AR	J_c (A mm^{-2})
1	295	26.7	8.5	18.2	2234	1.07	6.10×10^4
2	325	27.8	9.5	18.3	2422	1.16	5.98×10^4
3	311	27.0	9.3	17.7	2288	1.08	5.85×10^4
4	274	26.7	8.9	17.8	2243	1.03	5.39×10^4
5	323	27.1	9.5	17.6	2308	1.15	5.96×10^4
6	306	27.7	9.1	18.6	2414	1.08	5.85×10^4
7	320	27.7	8.7	18.9	2408	1.18	6.38×10^4
8	234	27.4	7.2	20.2	2359	1.13	5.65×10^4
9	328	27.5	9.7	17.8	2378	1.05	5.89×10^4
10	335	27.9	9.7	18.3	2447	1.09	6.05×10^4
11	335	27.3	9.8	17.6	2347	1.08	6.00×10^4
12	337	28.3	9.3	18.9	2514	1.11	6.28×10^4
13	330	27.0	9.1	17.8	2286	1.20	6.31×10^4
14	331	27.8	8.7	19.1	2426	1.08	6.62×10^4
15	284	27.6	9.0	18.6	2398	1.13	5.50×10^4

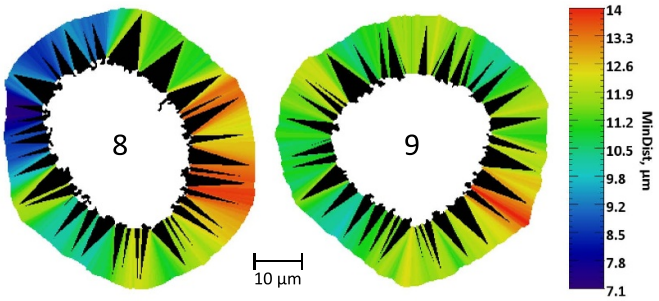

Figure 6. Minimum thickness of the A15 layer of two sub-elements of the RRP-Ti wire.

scans in the Meißner state at an applied external field of 5 mT (zero field cooled). Figure 7 shows a Meißner scan of the RRP-Ti wire at 5 mT and 16.5 K, where the sub-elements retain the same numbers as applied in figure 4.

From these results, it becomes apparent that different sub-elements show variations in the shielding capacity which can be related to differences in T_c, where sub-elements number 9 and 11 show exceptionally low shielding capacities, while sub-element number 7 shows a better performance. As discussed in the following section, differences in T_c can generally be understood as differences in the local Sn content in the inner parts of the A15 layer of the sub-elements, where the Sn content and T_c reach their maximum values.

3.5. *Influence of local composition on sub-element T_c*

Differences in T_c that became apparent in figure 7 can be related to variations in the elemental composition, since it is well known that such inhomogeneities significantly impact the superconducting properties [2, 3, 11]. The influence of the additive content on T_c in ternary RRP and PIT wires is not well understood. In [12] it was shown that the addition of 10 wt.% Ta to bronze processed Nb_3Sn wires reduced T_c by about 1 K, depending on the heat treatment. In [13] it was found that small additions of Ti (1 at.%) or Ta (3 at.%) slightly increased the value of T_c (by 0.2–0.4 K) above that of pure

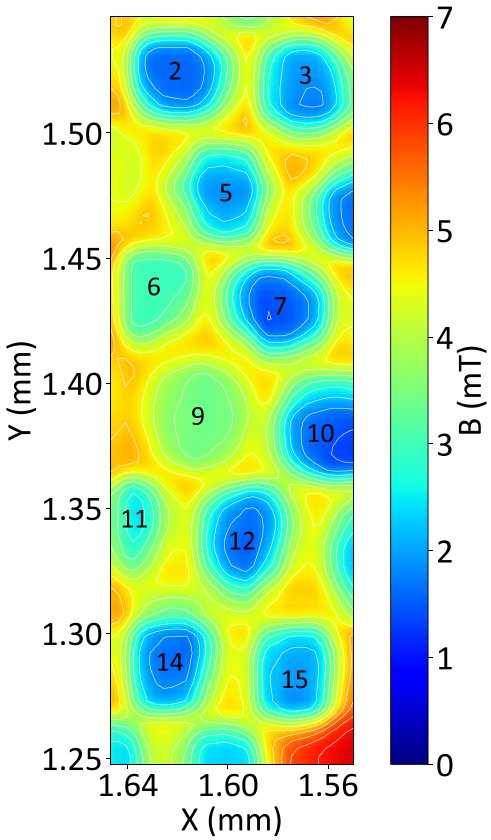

Figure 7. Meißner scan of the RRP-Ti wire at 5 mT and 16.5 K.

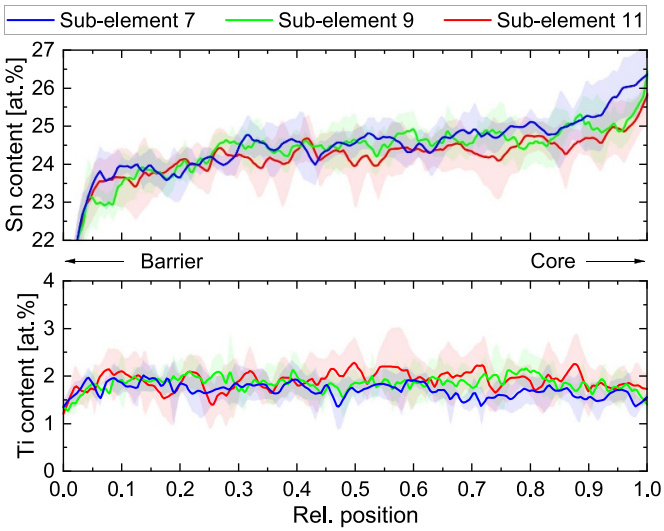

Figure 8. Comparison of the Sn and Ti content distributions of different sub-elements of the RRP-Ti wire. The standard deviations are indicated by the shaded areas.

Nb_3Sn in bronze processed wires. However, additions of larger amounts of these elements substantially decreased T_c. Furthermore, small additions of these elements significantly increased the upper critical field B_{c2} above that of pure Nb_3Sn. The maximum value of B_{c2} obtained as a consequence of these additions was 27 T at 4.2 K, for additions of 1.5 at.% Ti or 4 at.% Ta, compared with a value of 23.5 T of the unalloyed Nb_3Sn. Additional discussions about the variation of T_c and B_{c2} in Ti and Ta alloyed Nb_3Sn can be found in [14].

The T_c measured by SHPM can be limited by local minima of the Sn content near the sub-element centre which inhibit continuous shielding currents at higher temperatures. Due to this dependence, EDX line scans were carried out on sub-elements number 7, 9 and 11 in order to confirm a difference in the Sn content, which was suspected from the Meißner shielding shown in figure 7. On each sub-element, multiple line scans were performed in the radial direction and averaged. The results are summarized in figure 8, where the Cu content was factored out for an accurate comparison of the Sn content.

These results suggest a correlation between the Sn content and differences in T_c between the sub-elements. Sub-elements number 9 and 11, which showed a poor T_c performance in the Meißner scans, also showed a lower average Sn content than the better performing sub-element number 7 and indications of locations with exceptionally low values. Especially towards the inner parts at relative positions above 0.9, sub-element 7 shows higher Sn contents, while the Ti content shows slightly lower values compared to the other sub-elements.

The EDX signal of Nb_3Sn at an accelerating voltage of 10 kV originates from only up to a few hundred nm below the sample surface [4] and differences in the measured T_c between sub-elements could additionally be attributed to longitudinal variations of the Sn content over a larger distance along the wire axis. Such longitudinal variations could impact the magnetic signal measured by SHPM due to current flow in deeper sample layers.

3.6. Longitudinal variations in the elemental composition and geometry

In order to examine possible longitudinal gradients of the Sn concentration, an EDX analysis was performed on a longitudinally polished RRP-Ti wire sub-element close to the wire centre which shows practically no twisting, contrary to the outer sub-elements. The EDX data are shown in figure 9, where variations in the Sn content that are clearly larger than the noise become apparent. Additionally, much care was taken to measure parallel to the wire axis to obtain information of the change in Sn content along the wire axis only, without any influence from radial gradients. From these results, it can be concluded that there are significant changes of the A15 Sn content along the wire axis of over 1.5 at.%, in this case within a distance of less than 30 μm. The observed radial and longitudinal variations can therefore both impact the distribution of T_c.

Aside from variations of the Sn content, longitudinal variations of the A15 geometry could also impact the superconducting properties. An evaluation of geometric variations along the wire axis is shown in figure 10, where the distance between the outer and the inner border of the A15 layer was measured at multiple points in a SEM image of the transversal cross section of an RRP-Ti sub-element. Longitudinal variations of the A15 layer thickness up to 2 μm were observed within the longitudinal distance of 60 μm, which equals a

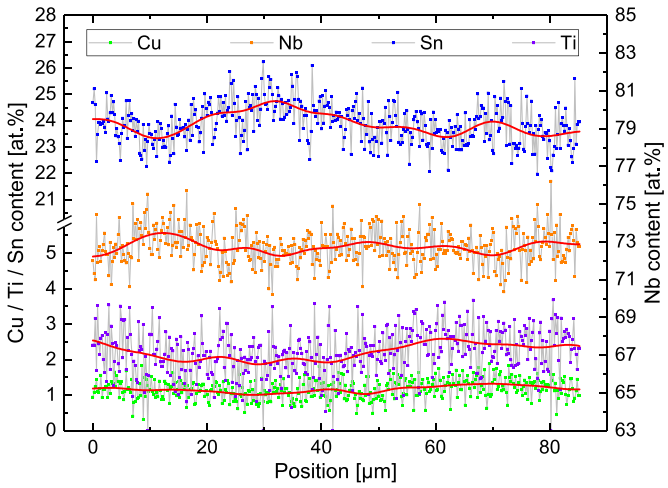

Figure 9. EDX line scan along the RRP-Ti wire axis showing longitudinal variations in the elemental composition. The data were smoothed by FFT filtering as marked by the solid lines in order to reduce the noise of the signal.

reduction of the maximum thickness by 16%. Furthermore visible is the presence of inter-filamentary material within the A15 phase that stretches over a distance of more than 50 μm, which results from the manufacturing process of RRP wires that makes use of stacked Nb filaments.

The determined longitudinal variations of the Sn content and geometry along the wire axis can have an impact on the performance of the wire by limiting the superconducting properties locally. It is obvious that no conclusions can be made about the entire wire over a long distance from only measuring a few μm along the axis. However, given that in this study, considerable inhomogeneities in wires of small lengths up to 3 mm were determined, it can be expected that in practical wires of longer lengths the superconducting properties might be even more inhibited, since they are determined by the worst performing region. If such large variations were present in multiple sub-elements within short distances along the axis, it would have a significant impact on the wire performance.

3.7. Global correlation of T_c and Sn content

This section aims to establish statistics of the dependency of T_c on the Sn content that is valid for the entire wire cross section by averaging multiple sub-elements, contrary to the investigations of the previous sections, where differences between sub-elements were compared. For the investigations described in this section, the PIT-Ta wire was more suited since it exhibits a greater homogeneity of geometry and Sn content between different sub-elements compared to the RRP-Ti wire, which results in a lower standard deviation of the EDX statistics and the values of the sub-element diameters being more comparable. SHPM scans were performed on a transversal cross section of the PIT-Ta wire in the Meißner state at different temperatures and a small applied magnetic field of 5 mT. Due to the Nb barrier being superconducting below about 9 K [15], the lower temperature limit of our measurements was set to 10 K. The scans of the PIT-Ta wire were used in combination with radial EDX line scans of this wire in order to determine the dependence of T_c on the Sn content.

As a first step, the shielded area was analysed at each temperature as described in [15], where the contour lines at 50% of the applied field were evaluated. The reason for not evaluating the contour lines at 100% of the applied field is that due to the background signal between the sub-elements, the contour lines would then overlap and not form closed loops. Figure 11 shows the contour plots of the PIT-Ta sub-elements at 2.5 mT and different temperatures. The size of the shielded areas decreases with increasing temperature and confirm a T_c distribution due to the radial gradient of the Sn concentration, which previous studies have determined using magnetic and calorimetric methods on various Nb_3Sn wires [16–18].

The average radii of the shielded areas (assuming a circular shape) were then correlated with the Sn content at each position, which was acquired from EDX line scans. These radii were acquired by scaling the contour plots at 2.5 mT to the value at 5 mT, which corresponds to the applied field during the measurements and therefore defines the outer border of the shielded area. For the evaluation of our measurements, in order to obtain this scaling factor, a reference point had to be chosen. A Boltzmann function was proposed in [11], which accurately describes the dependence of T_c on the Sn content determined experimentally in previous studies. The assumption for the reference point was made that a T_c of 10 K, our lower temperature limit, corresponds to a Sn content of 21.35 at.% as described by the Boltzmann function, therefore the values of the shielding radii at this temperature have to correspond to the position of this given Sn content in the A15 layers of the sub-elements. The correlation of the shielding radii with the Sn content was therefore achieved by extending the average values of the radii at all temperatures from 2.5 mT to 5 mT by adding the same constant value so that the radius at 10 K corresponds to a Sn content of 21.35 at.%. At this position in the A15 layer, T_c is 10 K and the shielding radii at this temperature and 5 mT are located here, at the border between the superconducting and normal conducting areas. For the remaining temperatures, the shielding radii at 5 mT are then known as they are scaled by adding the same value as at 10 K, after which they are correlated with the Sn content at the respective positions. The lower phase limit of Nb_3Sn is an atomic Sn content of 18% [11], which corresponds to the outer A15 layer radius.

Figure 12 shows the variation of the Sn content across the A15 layer of the PIT-Ta wire averaged over 10 EDX line scans, and the corresponding critical temperature at different points that was obtained through correlation with the shielding radii. The PIT wire analysed in [18] has a similar sub-element diameter and heat treatment, and a similar profile of Sn concentration was reported. It is well known and also discussed in that reference that PIT sub-elements show different grain morphologies. The coarse grains near the core that possess the highest Sn contents and highest T_c as seen in figure 12 do not significantly contribute to the current transport. These coarse grains

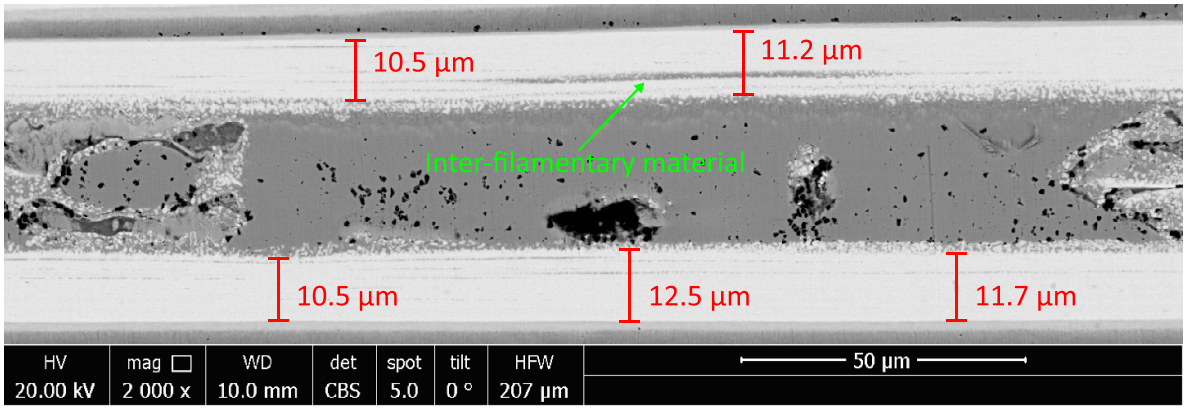

Figure 10. SEM image taken with the BSE detector of the longitudinal cross section of a single RRP-Ti sub-element showing variations of the A15 thickness along the wire axis.

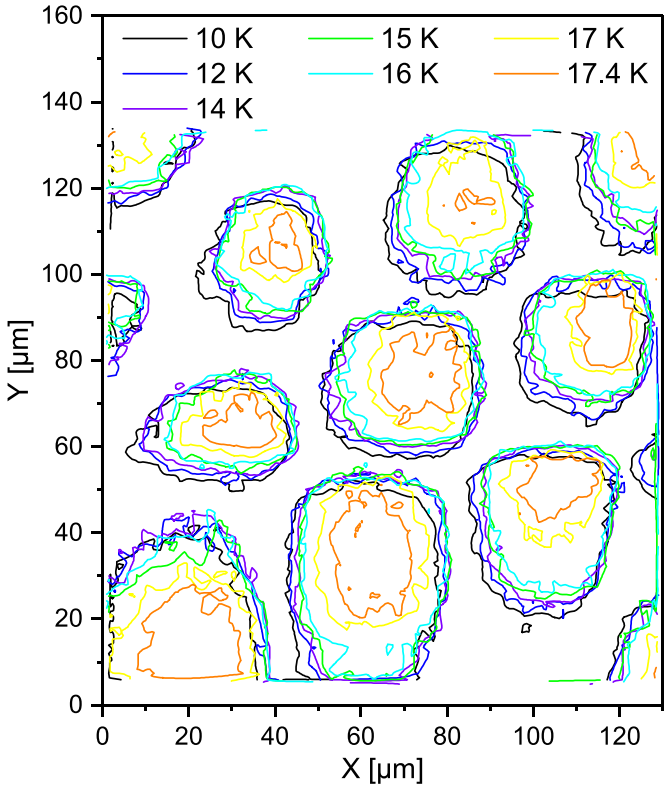

Figure 11. Contour plots of PIT-Ta sub-elements at 2.5 mT for an applied field of 5 mT and different temperatures.

are therefore not particularly interesting from a superconducting viewpoint. Regardless, the results of the analyses of Sn content and T_c in this region are useful for the determination of the correlation between these properties. The same analysis as described for the PIT-Ta wire was also conducted for the RRP-Ti wire and the result is shown in the same figure.

Through correlating the Sn content that was obtained using EDX with the distribution of the critical temperature T_c that was obtained using SHPM scans in the Meißner state, it is possible to assess the dependence of the critical temperature T_c on the Sn content as shown in figure 13, which is displayed for both investigated wire types. The resulting dependence shows a good agreement with the Boltzmann function found in [11]. Additionally, the linear function displayed in the same publication was included in figure 13, which also shows a reasonable fit to our data. One thing to note is the fact that the dependences in [11] describe the binary Nb_3Sn system, while the samples investigated here contain Ta and Ti, respectively. The influence of Ta and Ti on the dependence of T_c in RRP and PIT wires is not well known as discussed in section 3.5, but due to the good agreement between our data and the literature, we have no reason to assume that the addition of Ta and Ti is drastically altering the established dependence.

3.8. *Influence of Sn gradients on J_c*

As outlined in section 2.5, simulations were carried out to investigate the influence of the Sn concentration gradient on the critical current density J_c. The maximum Sn content of the initial profile, which matches the experimentally investigated wire in terms of the $J_c(B,T)$ dependence, was 24.4 at.%. Its Sn gradient in the linear region, which spans most of the A15 area except for a steep fall-off at the barrier, was set to a reference value of 0.1 at.% μm^{-1} that is comparable to experimentally observed values. In subsequent simulation runs, the Sn gradient was varied between 0% and twice the reference value of the original profile while keeping the maximum Sn content fixed. In each case the average transport J_c at 4.2 K and 16 T, and at 10 K in self-field was calculated.

The results of the simulations are presented in figure 14, which shows the relative variation of J_c when the Sn gradient is altered. The reason for the decline of J_c for small gradients at 4.2 K and 16 T is that the maximum Sn content is slightly above the value where B_{c2} is maximized, which has a large impact at high fields.

According to the simulation results, a reduction of the radial Sn gradient by 50% would lead to an increase in J_c by almost 5% at 4.2 K and 16 T, which is without considering all the other inhomogeneities that may be present. Furthermore, the simulation results for 10 K and self-field indicate that even a small J_c decrease measured by SHPM under these conditions can signify a substantial reduction in J_c at the much higher fields required for application in future particle accelerators.

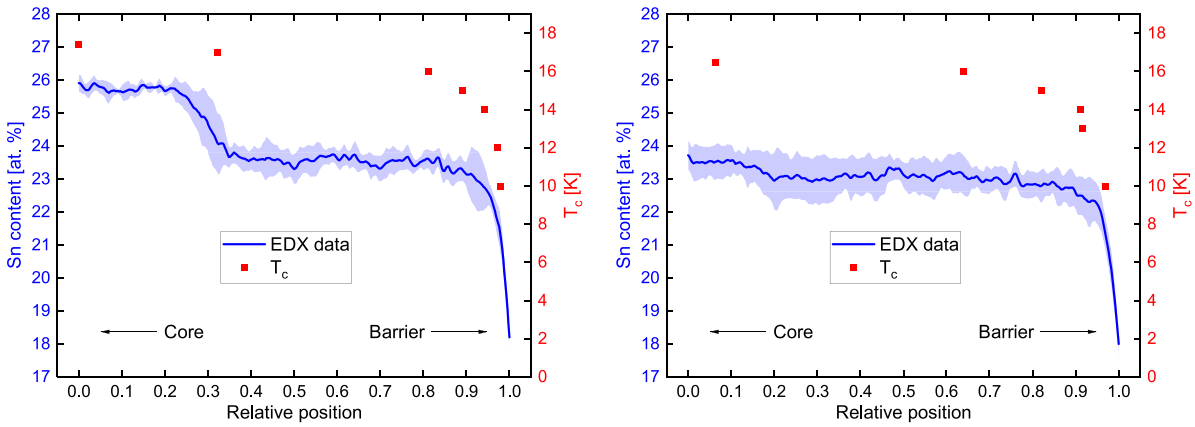

Figure 12. Statistics of EDX line scans across A15 phase of PIT-Ta (left) and RRP-Ti (right) sub-elements and position of shielding radii at different temperatures. The shaded area indicates the standard deviation.

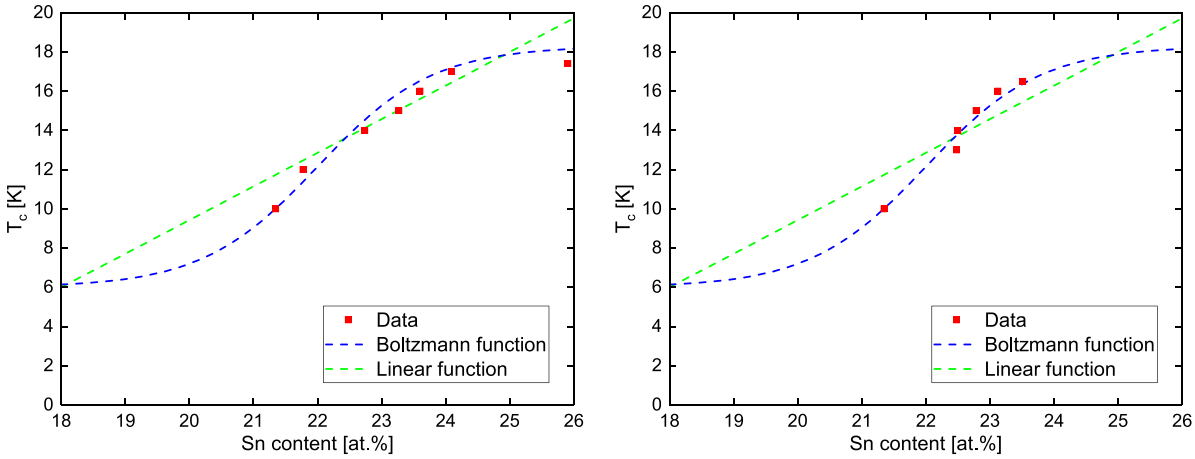

Figure 13. Dependence of T_c on the Sn content in the PIT-Ta wire (left) and RRP-Ti wire (right) together with the functions described in [11].

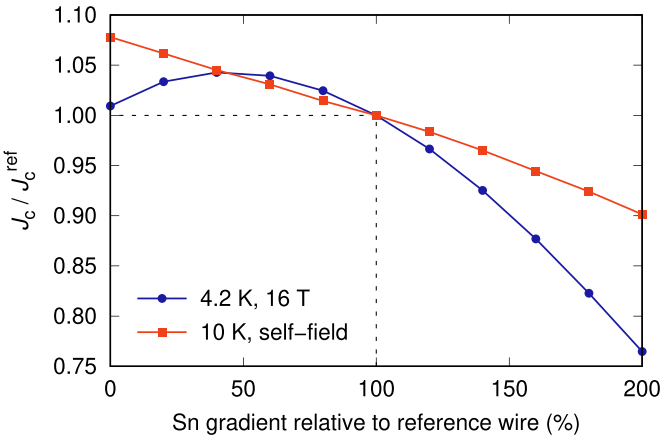

Figure 14. Simulation of the impact of different Sn gradients on J_c.

4. Conclusions

In this study, we demonstrated the combined use of SEM, EDX and SHPM to determine inhomogeneities in RRP and PIT Nb_3Sn wires. We acquired information about sub-element area and aspect ratio distributions, remanent fields and their correlation with the microstructure, differences in J_c between sub-elements, variations in the sub-element T_c, longitudinal variations in the elemental composition and geometry, the correlation of T_c and Sn content and the influence of Sn gradients on J_c.

The results of our study can be summarized as follows:

(a) The sub-element area distributions of the investigated wires can be described by Gaussian functions and in the present study showed variations of up to 20% between sub-elements.

(b) The local remanent field values of a Hall scan were used in combination with geometric data acquired by SEM in order to calculate J_c of the A15 phase of each sub-element. The resulting J_c values show variations of up to around 20% between sub-elements.

(c) We observed differences in the shielding capacities and therefore T_c in the Meißner scans of the RRP-Ti wire. The variations in T_c can be attributed to compositional inhomogeneities of the A15 phase, which were confirmed by EDX analyses.

(d) We investigated and confirmed longitudinal variations of the Sn content of the A15 layer along the RRP-Ti wire axis of up to 1.5 at.% that can additionally explain the differences in T_c between sub-elements. We furthermore found considerable longitudinal variations of the A15 thickness along the wire axis, up to 2 μm, that can inhibit the current locally.
(e) SHPM scans in the Meißner state at different temperatures confirmed a radial T_c gradient inside the sub-elements due to a radial Sn gradient. The correlation of the shielding radii with the Sn content obtained by EDX analysis yielded the dependence of T_c on the Sn content, which was found to be consistent with existing literature data.
(f) Simulations of the influence of Sn gradients on J_c showed that an optimization of the radial Sn gradient inside sub-elements can result in a J_c increase, and that even small differences in J_c at low fields can signify substantial differences at the higher fields required for application in future particle accelerators.

Aside from demonstrating the methods to analyse such inhomogeneities, it becomes apparent from this study that in current state-of-the-art wires there are geometric and compositional inhomogeneities between different sub-elements, inside single sub-elements, as well as longitudinally, which cannot be neglected. Given the magnitude of inhomogeneities found within short distances in this study, it is to be expected that they have a significant impact on the performance in practical wires. The performance of Nb_3Sn wires to be used in FCC magnets could therefore benefit from the reduction of these inhomogeneities.

Data availability statement

The data that support the findings of this study are available upon reasonable request from the authors.

Acknowledgments

This work was carried out with financial support from CERN within the FCC study under the Collaboration Agreement KE3194. The authors are grateful for funding the research at USTEM and Atominstitut and also acknowledge TU Wien University Library for financial support through its Open Access Funding Programme.

ORCID iDs

S Pfeiffer https://orcid.org/0000-0002-2085-0390
T Baumgartner https://orcid.org/0000-0002-2228-1072
S Löffler https://orcid.org/0000-0003-0080-2495
M Stöger-Pollach https://orcid.org/0000-0002-5450-4621
S C Hopkins https://orcid.org/0000-0002-0245-8627
M Eisterer https://orcid.org/0000-0002-7160-7331
J Bernardi https://orcid.org/0000-0002-4626-9246

References

[1] Amalia B *et al* 2019 The CERN FCC conductor development program: a worldwide effort for the future generation of high-field magnets *IEEE Trans. Appl. Supercond.* **29** 1–9
[2] Cooley L D, Fischer C M, Lee P J and Larbalestier D C 2004 Simulations of the effects of tin composition gradients on the superconducting properties of Nb_3Sn conductors *J. Appl. Phys.* **96** 2122–30
[3] Baumgartner T, Pfeiffer S, Bernardi J, Ballarino A and Eisterer M 2018 Effects of inhomogeneities on pinning force scaling in Nb_3Sn wires *Supercond. Sci. Technol.* **31** 084002
[4] Potts P J 1987 *A Handbook of Silicate Rock Analysis* (Dordrecht: Springer)
[5] Li Y and Gao Y 2017 GLAG theory for superconducting property variations with A15 composition in Nb_3Sn wires *Sci. Rep.* **7** 1133
[6] Fischer C M 2002 Investigation of the relationships between superconducting properties and Nb_3Sn reaction conditions in powder-in-tube Nb_3Sn conductors *Master's Thesis* University of Wisconsin-Madison
[7] Ferreira T, Hiner M, Rueden C, Miura K, Eglinger J and Chef B 2017 Bar scripts 1.5.1 (Zenodo) (available at: https://zenodo.org/record/495245)
[8] Lee P J 2018 ImageJ utilities: applied superconductivity center, NHMFL (available at: https://fs.magnet.fsu.edu/~lee/asc/ImageJUtilities/ASC_ImageJ_Utils.html)
[9] Chen I-G, Liu J, Weinstein R and Lau K 1992 Characterization of $YBa_2Cu_3O_7$, including critical current density J_c, by trapped magnetic field *J. Appl. Phys.* **72** 1013–20
[10] Baumgartner T, Eisterer M, Weber H W, Flükiger R, Bordini B, Bottura L and Scheuerlein C 2012 Evaluation of the critical current density of multifilamentary Nb_3Sn wires from magnetization measurements *IEEE Trans. Appl. Supercond.* **22** 6000604
[11] Godeke A 2006 A review of the properties of Nb_3Sn and their variation with A15 composition, morphology and strain state *Supercond. Sci. Technol.* **19** R68–R80
[12] Suenaga M, Aihara K, Kaiho K and Luhman T S 1980 Superconducting properties of (Nb, Ta)$_3$Sn wires fabricated by the bronze process *Advances in Cryogenic Engineering Materials* vol 26 (New York: Springer) pp 442–50
[13] Suenaga M, Welch D O, Sabatini R L, Kammerer O F and Okuda S 1986 Superconducting critical temperatures, critical magnetic fields, lattice parameters and chemical compositions of "bulk" pure and alloyed Nb_3Sn produced by the bronze process *J. Appl. Phys.* **59** 840–53
[14] Flükiger R, Uglietti D, Senatore C and Buta F 2008 Microstructure, composition and critical current density of superconducting Nb_3Sn wires *Cryogenics* **48** 293–307
[15] Baumgartner T, Hecher J, Bernardi J, Pfeiffer S, Senatore C and Eisterer M 2016 Assessing composition gradients in multifilamentary superconductors by means of magnetometry methods *Supercond. Sci. Technol.* **30** 014011
[16] Senatore C, Uglietti D, Abacherli V, Junod A and Flukiger R 2007 Specific heat, a method to determine the tc distribution in industrial Nb_3Sn wires prepared by various techniques *IEEE Trans. Appl. Supercond.* **17** 2611–4
[17] Senatore C, Abächerli V, Cantoni M and Flükiger R 2007 Distribution of Tc from calorimetry and the determination of Sn gradients in bronze Nb_3Sn wires with an internal and external Ti source *Supercond. Sci. Technol.* **20** S217–22
[18] Tarantini C, Segal C, Sung Z H, Lee P J, Oberli L, Ballarino A, Bottura L and Larbalestier D C 2015 Composition and connectivity variability of the A15 phase in PIT Nb_3Sn wires *Supercond. Sci. Technol.* **28** 095001